



Assessment of model assumptions and budget terms of the unsteady flamelet equations for a turbulent reacting jet-in-cross-flow



Wai Lee Chan^a, Hemanth Kolla^b, Jacqueline H. Chen^b, Matthias Ihme^{c,*}

^a Department of Aerospace Engineering, University of Michigan, Ann Arbor, MI 48109, USA

^b Sandia National Laboratories, Livermore, CA 94550, USA

^c Department of Mechanical Engineering, Stanford University, Stanford, CA 94305, USA

ARTICLE INFO

Article history:

Received 15 July 2013

Received in revised form 1 November 2013

Accepted 13 April 2014

Available online 5 May 2014

Keywords:

Flamelet modeling

Diffusion flame

Budget-analysis

Jet-in-cross-flow

Direct numerical simulation

ABSTRACT

An *a priori* analysis of the flamelet model for diffusion flames is conducted to systematically assess model assumptions that are associated with the asymptotic expansion, the omission of higher-order expansion terms, the consideration of preferential diffusion effects, and the one-dimensional flamelet representation. For this, a recent direct numerical simulation database of a reacting hydrogen/air jet-in-cross-flow (JICF) by Grout et al. [15,16] is used. The full flamelet equation for temperature, exact to the order of the Eulerian transport equation and general to different definitions of the mixture fraction, is derived. Analysis of mixture fraction conditioned profiles of temperature and scalar dissipation rate along the jet trajectory identified different ignition and flame stabilization scenarios on the windward and leeward sides of the reacting JICF. A balance analysis of the temperature flamelet equation is conducted to quantify contributions in flame-aligned and flame-orthogonal directions. Consistent with the flamelet assumption, it is shown that terms arising from scalar diffusion, heat-release, and species-diffusion-induced enthalpy flux are the dominant contributions, while the flame-aligned preferential diffusion promotes entrainment of heat into the flamelet structure. For the current JICF-configuration, it is found that contributions along the flame-orthogonal direction are on average negligible.

© 2014 The Combustion Institute. Published by Elsevier Inc. All rights reserved.

1. Introduction

The flamelet model is derived from an asymptotic analysis and considers a turbulent diffusion flame as an ensemble of laminar flame structures [1–3]. To first order, the structure of this flame is then characterized by a competition between reaction and diffusion processes, while other effects such as heat conduction and unsteadiness are negligible. At sufficiently large Damköhler numbers or sufficiently high activation energy, chemical reactions and heat transfer are confined to a thin reaction–diffusion layer. If the characteristic length-scale of this layer is smaller than that of the surrounding turbulence, turbulent structures are unable to penetrate or destroy the reaction zone. Therefore, the effect of turbulence in this so-called connected flame-zone regime results only in a deformation and stretching of the flame-structure. Flamelet-based combustion models enable the representation of complex reaction chemistry in terms of a reduced set of scalars, which typically consists of mixture fraction Z , scalar dissipation rate χ_Z , and reaction progress variable C . Other advantages of

flamelet-based combustion-models are the precomputation and pretabulation of the thermochemical state-space prior to the simulation, the consideration of turbulence/chemistry interaction using a probability-density function description, and the representation of detailed reaction chemistry of arbitrary complexity.

To obtain a coordinate-independent flamelet-formulation, several model assumptions are invoked. These assumptions can be related to: (i) the representation of the combustion facility; (ii) the description of transport and combustion-chemical processes; and (iii) the characterization of the flame-topology. In particular, approximations regarding the combustion facility include the consideration of isobaric heat-release, the description of the reactant-feed system, and adiabatic combustion approximations and associated implications about convective, conductive and radiative heat-exchange processes. Assumptions about equal species diffusivities, large Damköhler number-combustion regimes, and the omission of chemical processes that evolve on slow time scales can be categorized as combustion-chemical-transport approximations. Assumptions about the flame-structure include the flame representation in terms of canonical shear-layer or counterflow diffusion flame configurations and the omission of flame curvature and flamelet interaction effects.

* Corresponding author.

E-mail address: mihme@stanford.edu (M. Ihme).

Over recent years, several extensions of the flamelet model have been proposed to account for non-unity Lewis-number effects [4], flame curvature [5,6], multi-feed combustion [7–9], pressure-effects [10], processes that evolve on slow physicochemical time-scales due to radiation and pollutant formation [11], and unsteady processes [12–14].

The flamelet model has been successfully applied to simulations of turbulent diffusion flames, such as shear-layers, piloted, bluff-body and swirl-stabilized jet flames, and gas-turbine combustors. While previous investigations focused largely on the validation of models for large-eddy simulation (LES) and Reynolds-averaged Navier–Stokes (RANS) methods, underlying assumptions that are associated with the derivation of the flamelet formulation have so far not been rigorously evaluated. In particular, fundamental assumptions about the omission of higher-order expansion terms, contributions along flame-orthogonal directions, the Lagrangian flamelet topology, and the representation of combustion-physical mechanisms arising from flame propagation, preferential diffusion, and strain processes are only partially assessed. The main reason for this is that these aspects cannot be fully addressed through theoretical and experimental investigations. Instead, direct numerical simulations (DNS) of relevant flame configurations are necessary to systematically examine these underlying assumptions. Therefore, the objective of this study is to address this issue by examining contributions of higher-order expansion terms, preferential diffusion, transient effects, and scalar dissipation rate on the flame structure in the context of a Lagrangian analysis of the flamelet equations. This analysis is conducted in the context of an *a priori* study of a DNS-database of a reacting jet-in-cross-flow (JICF), recently performed by Grout et al. [15,16].

JICF-configurations are of practical relevance as fuel-injection systems for high-speed propulsion applications and as mixing strategies in gas-turbine combustors. JICFs are characterized by complex vortical structures that control the mixing, ignition, and combustion phenomena. Because of the vortical structures that are associated with shear layers and horseshoe vortices near the injector and the formation of counter-rotating and wake vortices in the jet far-field [17], this configuration exhibits significantly more complex structures than uni-directional jet-flow configurations. Furthermore, the flame stabilization in reacting JICFs is often affected by an interplay between different mechanisms, involving autoignition, partially-premixed flame behavior, and vortex-induced recirculation modes. The reacting JICF-configuration and the DNS-database considered in the present investigation are summarized in the next section. The flamelet transformation, distinction between flame-aligned and flame-orthogonal contributions, and details regarding the diagnostics for evaluating the flamelet topology are presented in Section 3. Results of the flamelet analysis are discussed in Section 4, and the paper finishes with conclusions.

2. DNS-database and reactive JICF-configuration

In the present study, a DNS-database of an isobaric reacting JICF at atmospheric pressure is used to assess the validity of individual assumptions of the flamelet formulation. This DNS was performed by Grout et al. [15,16]. The reacting JICF-configuration consists of a fuel jet that exits from a circular nozzle into a turbulent cross flow of preheated air at a temperature of 750 K. The jet exit velocity is $U_j = 250$ m/s and the jet diameter is 1 mm, resulting in a nominal jet-exit Reynolds number of approximately 4000. The fuel jet consists of a mixture of 70% hydrogen and 30% nitrogen by volume at a temperature of 420 K. The velocity of the cross-flow is $U_{cf} = 55$ m/s. The velocity and momentum flux ratio for this configuration are $U_j/U_{cf} = 4.5$ and $\rho_j U_j^2 / \rho_{cf} U_{cf}^2 = 12.55$, respectively. The reaction chemistry is represented by a detailed hydrogen/air

mechanism consisting of 9 species and 19 elementary reactions [18]. The stoichiometric mixture fraction is $Z_{st} = 0.169$. In the following, all results are presented in non-dimensional form, using values for reference temperature, $T_{ref} = 300$ K, time, $t_{ref} = 2.7 \times 10^{-5}$ s, length, $l_{ref} = 1.5 \times 10^{-2}$ m, and density, $\rho_{ref} = 0.47$ kg/m³. These reference quantities are consistent with the DNS [15,16], in which all variables are related to the acoustic scale at ambient condition.

Figure 1 shows the non-dimensional mean temperature from the JICF-DNS, and the solid curve denotes the stoichiometric isocontour. The flamelet-analysis is performed in terms of a jet-local coordinate system, which is represented by the jet trajectory η and the arc-length coordinate ξ along the stoichiometric isocontour at a plane normal to η . In the following, this coordinate system is constructed from the mean mixture fraction field and is used to uniquely identify the flamelet-anchoring points for the subsequent analysis.

Following the procedure outlined in Ref. [16], the mean jet-trajectory is computed as the solution to a Laplace problem, $\nabla^2 \eta = 0$, inside the volume that is confined by the mean stoichiometric mixture fraction $Z = 0.05$. This volume has prescribed boundary conditions at the jet exit ($\eta = 0$) and the end of the computation domain ($\eta = 1$). While this method defines η as a field-variable, only the trajectory along the center of the volume is used for the flamelet-analysis. This trajectory is illustrated in Fig. 1.

For any given cross-sectional plane of η , ξ is then evaluated from the path-integral along the stoichiometric isocontour:

$$\xi = \frac{1}{\Xi} \int \sqrt{r_{st}^2 + \left(\frac{dr_{st}}{d\theta}\right)^2} d\theta, \quad (1)$$

where r_{st} is the radial location of the stoichiometric mixture surface, and Ξ is the circumference, so that ξ is normalized with $\xi = 0$ corresponding to the windward side of the jet and $\xi = 0.5$ denoting the leeward side for an axisymmetric jet cross-section.

3. Mathematical formulation and diagnostics

3.1. Mixture fraction

Energy and species transport in turbulent diffusion flames are affected by a competition between reaction, advection, and transport on molecular and turbulent scales. While turbulent transport typically controls mixing, preferential diffusion effects can become relevant at low Reynolds number flow conditions and for mixtures involving species with different molecular weights. To consider preferential diffusion effects in the present investigation, we utilize the mixture fraction formulation due to Bilger et al. [19]. This formulation is based on the elemental mass fractions and can be written as:

$$Z = \frac{Z - Z_0}{Z_1 - Z_0} \quad \text{with} \quad Z = \sum_{\beta=1}^{N_e} \gamma_{\beta} \sum_{\alpha=1}^{N_s} \frac{n_{\alpha\beta} W_{\beta}}{W_{\alpha}} Y_{\alpha}, \quad (2)$$

where $n_{\alpha\beta}$ denotes the number of atoms of element β in species α , γ_{β} is a weighting factor, and W_{α} and Y_{α} are the molecular weight and the mass fraction of species α , respectively. Subscripts “0” and “1” refer to conditions in the oxidizer stream and in the fuel stream. With this definition, the following transport equation for Z can be derived from the species-conservation equations [20]:

$$\rho \frac{\partial Z}{\partial t} + \rho \mathbf{u} \cdot \nabla Z = \nabla \cdot (\rho D_Z \nabla Z) + \mathcal{E}, \quad (3)$$

where the preferential diffusion term \mathcal{E} has the form:

$$\mathcal{E} = -\frac{1}{Z_1 - Z_0} \sum_{\beta=1}^{N_e} \gamma_{\beta} \left(\sum_{\alpha=1}^{N_s} \frac{n_{\alpha\beta} W_{\beta}}{W_{\alpha}} \nabla \cdot \mathbf{j}_{\alpha} \right) - \nabla \cdot (\rho D_Z \nabla Z). \quad (4)$$

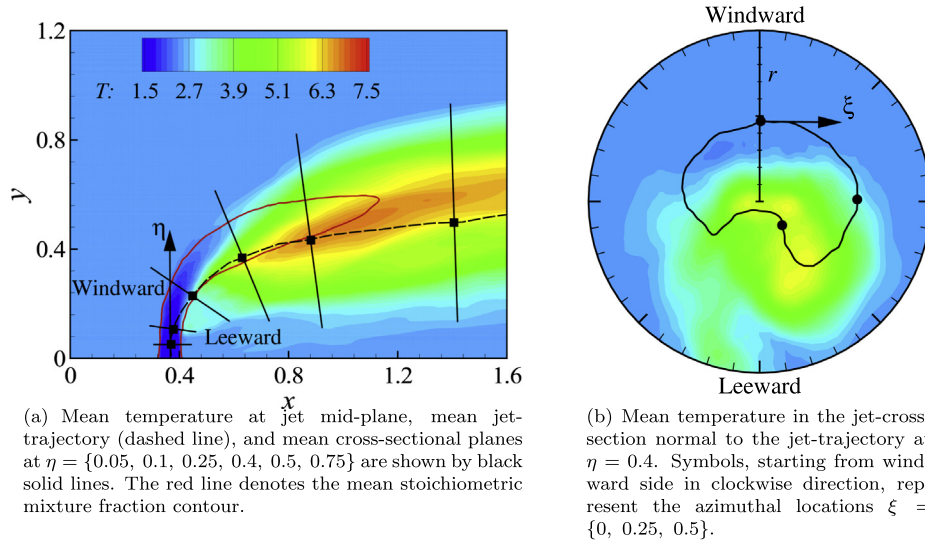


Fig. 1. Non-dimensional mean temperature field from DNS-database along (a) jet mid-plane and (b) cross-section normal to jet trajectory at $\eta = 0.4$. Reference coordinate system, parameterizing jet trajectory and azimuthal direction, is denoted by η and ξ , and is evaluated from the mean stoichiometric isosurface. The flamelet analysis is performed at cross-sections $\eta = \{0.05, 0.1, 0.25, 0.5, 0.75\}$, as shown in (a).

The mass diffusion flux of species α in the DNS is evaluated using Fick's law, which is written as:

$$\mathbf{j}_\alpha = -\frac{\rho D_\alpha}{Le_\alpha} (\nabla Y_\alpha + Y_\alpha \nabla \ln W), \quad (5)$$

and

$$Le_\alpha = \frac{\lambda}{c_p \rho D_\alpha} = \frac{D_z}{D_\alpha} \quad (6)$$

is the Lewis-number of species α .

In the DNS-database, the mixture fraction is evaluated from Eq. (2), and therefore implicitly contains effects of preferential diffusion. As such, Z is a function of species composition, and cannot be considered as an independent scalar in the flamelet analysis. To consider this in the present study, a flamelet equation that is formulated in terms of Bilger's mixture fraction is derived in Section 3.3.

In this context it is noted that the preferential diffusion term \mathcal{E} becomes zero for unity Lewis-number problems or if Z is defined following the formulation due to Pitsch and Peters [4]. Under these conditions, Eq. (3) and the flamelet equation, shown in Section 3.3, will reduce to their respective conventional forms. Therefore, \mathcal{E} is a convenient quantity to account for different definitions of the mixture fraction.

3.2. Evaluation of flamelet topology

The flamelet equations are formulated with respect to a flame-local coordinate system that is attached to the mixture fraction iso-surface and aligned with the mixture fraction gradient. In the following analysis, we introduce an orthogonal coordinate system that is spanned by the covariant basis vectors $\hat{\mathbf{n}}$, $\hat{\mathbf{s}}$, and $\hat{\mathbf{t}}$, which are defined through the following expressions:

$$\hat{\mathbf{n}} = \frac{\nabla Z}{|\nabla Z|}, \quad \hat{\mathbf{s}} = \frac{\hat{\mathbf{n}} \times \hat{\mathbf{e}}}{|\hat{\mathbf{n}} \times \hat{\mathbf{e}}|}, \quad \hat{\mathbf{t}} = -\hat{\mathbf{n}} \times \hat{\mathbf{s}}, \quad (7)$$

where $\hat{\mathbf{e}}$ is an auxiliary vector that is not aligned with the mixture fraction gradient, and $\hat{\mathbf{n}}$ is the normal vector of the mixture fraction iso-surface pointing towards the fuel mixture.

In the flamelet-formulation, all quantities and derivatives along the flame-aligned direction $\hat{\mathbf{n}}$ are associated with the flamelet-structure and all orthogonal contributions along the plane that is

spanned by the vectors $\hat{\mathbf{s}}$ and $\hat{\mathbf{t}}$ are considered to be small compared to the leading order terms.

The spatial flamelet-structure can be evaluated by integrating the following equation:

$$d\mathbf{x} = \hat{\mathbf{n}} \frac{dZ}{|\nabla Z|}. \quad (8)$$

This relation maps the mixture fraction space to the physical space, and is used to extract flamelet profiles from the DNS-database.

Technical details regarding the evaluation of the instantaneous flamelet structure are presented by considering Fig. 2, which shows the instantaneous stoichiometric isocontour (red) at the jet mid-plane. Beginning with the specification of a coordinate location (η, ξ) , which defines a specific point on the mean stoichiometric surface (shown by crosses in Fig. 2b), so-called rays (dashed lines) are constructed. These rays are traversed until the outermost intersection point with the instantaneous stoichiometric surface is found (shown by open circles in Fig. 2b). This intersection defines the anchoring point of the instantaneous flamelet, and corresponds to a projection onto the mean stoichiometric surface. With this starting point, Eq. (8) is then integrated along the fuel-lean and fuel-rich direction to determine the geometric structure of this particular flamelet. Integration is terminated when a stationary point in the mixture fraction field is reached. This algorithm results in a robust method for obtaining a singly-connected flamelet with well-defined end-points. Instances that result from multiple intersections with the stoichiometric contour or the absence of an intersection point are excluded from the analysis.

The arclength ζ along the instantaneous flamelet structure is computed by taking the dot-product of $\hat{\mathbf{n}}$ and Eq. (8). Written in differential form, this relation is:

$$d\zeta = \hat{\mathbf{n}} \cdot d\mathbf{x} = \frac{dZ}{|\nabla Z|}. \quad (9)$$

In the present implementation, this equation is evaluated by path-integrating along the direction of $\hat{\mathbf{n}}$. The origin of the arclength is then shifted so that $\zeta = 0$ is aligned with the stoichiometric mixture, while $\zeta < 0$ and $\zeta > 0$ correspond to fuel-lean and fuel-rich mixtures, respectively.

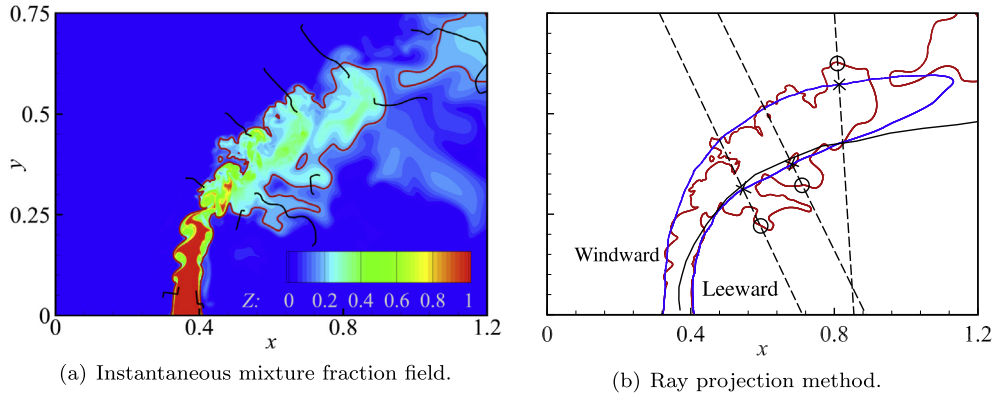


Fig. 2. Schematic illustration of the flamelet extraction procedure; (a) instantaneous mixture fraction field and stoichiometric isocontour (red) along the jet mid-plane; black curves represent instantaneous flamelets that are obtained using the projection algorithm summarized in (b): starting with the η - ζ intersection points on the mean stoichiometric surface (crosses), rays (dashed lines) are constructed and then traversed to find the outermost intersection points with the instantaneous stoichiometric surface (open symbols), thereby defining the instantaneous flamelet anchoring points. Beginning at these points, Eq. (8) is then integrated along fuel-rich and fuel-lean directions to construct the instantaneous flamelet-structure (shown in black in (a)). (For interpretation of the references to color in this figure legend, the reader is referred to the web version of this article.)

3.3. Flamelet equations

The focus of this study is on the temperature equation, which is written as:

$$\rho c_p \left(\frac{\partial T}{\partial t} + \mathbf{u} \cdot \nabla T \right) = \nabla \cdot (\lambda \nabla T) + \dot{\omega}_T + \sum_{\alpha=1}^{N_s} \rho c_{p,\alpha} \frac{D_z}{Le_\alpha} (\nabla Y_\alpha + Y_\alpha \nabla \ln W) \cdot \nabla T, \quad (10)$$

where, consistent with the DNS-solver [21], contributions due to radiation are neglected. Effects of acoustic pressure fluctuations and viscous work, which are contained in the compressible flow-field solution, are also omitted in the present analysis because they scale with the square of the Mach number. This appears to be a reasonable assumption due to the low-Mach number and isobaric operating conditions. Terms on the right-hand-side (RHS) of Eq. (10) are, respectively, the heat conduction, the heat-release rate, and the species-diffusion-induced enthalpy flux.

The flamelet equation is then derived by introducing an orthonormal coordinate system that is locally attached to the isosurfaces of mixture fraction [2]:

$$(t, \mathbf{x}) \rightarrow (\tau, Z(t, \mathbf{x}), Z_2(t, \mathbf{x}), Z_3(t, \mathbf{x})), \quad (11)$$

where Z_2 and Z_3 are the coordinates that are aligned with $\hat{\mathbf{s}}$ and $\hat{\mathbf{t}}$. The corresponding transformation operators can then be written as:

$$\frac{\partial}{\partial t} \rightarrow \frac{\partial}{\partial \tau} + \frac{\partial Z}{\partial t} \frac{\partial}{\partial Z} - (\mathbf{u} - (\mathbf{u} \cdot \hat{\mathbf{n}}) \hat{\mathbf{n}}) \cdot \nabla, \quad (12a)$$

$$\nabla \rightarrow \nabla Z \frac{\partial}{\partial Z} + \nabla_\perp, \quad (12b)$$

where τ is the Lagrangian flamelet time and ∇_\perp denotes the gradient in the flame-orthogonal direction. The last term, appearing on RHS of Eq. (12a), represents the Lagrangian flamelet velocity along the mixture fraction isosurface. This term stems from the fact that the transformed coordinate system convects with the velocity of the mixture fraction isosurface, which is given by Gibson [22]. It should be noted that Gibson's velocity applies to a point of the isosurface, not that of the flow, thus differentiating the current Lagrangian flamelet formulation from a conventional particle-tracking frame. In addition, as pointed out by Klimenko [23], consideration of the last term in Eq. (12a) will constitute a flamelet formulation that is coordinate-invariant and consistent with conditional moment closure equations.

After applying operators (12) to the temperature transport Eq. (10), the following flamelet equation is obtained:

$$\frac{\partial T}{\partial \tau} = \underbrace{(\mathcal{J}_1^Z + \mathcal{J}_2^Z + \mathcal{J}_3^Z + \mathcal{J}_5^Z)}_{\text{Flame-aligned contribution}} + \underbrace{(\mathcal{J}_4^\perp + \mathcal{J}_5^\perp)}_{\text{Flame-orthogonal contribution}}. \quad (13)$$

This equation is formulated in a Lagrangian reference frame, moving along the stoichiometric mixture fraction isosurface. The first term in brackets on the RHS contains leading-order flamelet-contributions along the mixture fraction direction, $\hat{\mathbf{n}}$. These contributions can be written as:

$$\mathcal{J}_1^Z = \frac{\chi_Z}{2} \frac{\partial^2 T}{\partial Z^2}, \quad (14a)$$

$$\mathcal{J}_2^Z = \frac{\dot{\omega}_T}{\rho c_p}, \quad (14b)$$

$$\mathcal{J}_3^Z = \frac{\chi_Z}{2c_p} \left\{ \frac{\partial c_p}{\partial Z} + \sum_{\alpha=1}^{N_s} \frac{c_{p,\alpha}}{Le_\alpha} \left(\frac{\partial Y_\alpha}{\partial Z} + Y_\alpha \frac{\partial \ln W}{\partial Z} \right) \right\} \frac{\partial T}{\partial Z}, \quad (14c)$$

$$\begin{aligned} \mathcal{J}_5^Z &= -\frac{\varepsilon^Z}{\rho} \frac{\partial T}{\partial Z} \\ &= -\frac{1}{Z_1 - Z_0} \sum_{\beta=1}^{N_e} \gamma_\beta \sum_{\alpha=1}^{N_s} \frac{n_{\alpha\beta} W_\beta}{W_\alpha} \left\{ \frac{\chi_Z}{2Le_\alpha} \left(\frac{\partial^2 Y_\alpha}{\partial Z^2} + Y_\alpha \frac{\partial^2 \ln W}{\partial Z^2} + \frac{\partial Y_\alpha}{\partial Z} \frac{\partial \ln W}{\partial Z} \right) \right. \\ &\quad \left. + \frac{\chi_Z}{4Le_\alpha} \left(\frac{\partial \ln \rho D_z}{\partial Z} - 2 \frac{\partial \ln Le_\alpha}{\partial Z} + \frac{\partial \ln \rho \chi_Z}{\partial Z} \right) \left(\frac{\partial Y_\alpha}{\partial Z} + Y_\alpha \frac{\partial \ln W}{\partial Z} \right) \right\} \frac{\partial T}{\partial Z} \\ &\quad + \frac{\chi_Z}{4} \left(\frac{\partial \ln \rho D_z}{\partial Z} + \frac{\partial \ln \rho \chi_Z}{\partial Z} \right) \frac{\partial T}{\partial Z}. \end{aligned} \quad (14d)$$

Terms denoted by the superscript “ \perp ” arise from contributions that are perpendicular to the flame-aligned direction, and are commonly neglected in the asymptotic flamelet limit. These terms are:

$$\begin{aligned} \mathcal{J}_4^\perp &= D_z \left(\nabla Z \frac{\partial}{\partial Z} + \nabla_\perp \right) \cdot \nabla_\perp T + \frac{1}{\rho c_p} \nabla_\perp \cdot (\rho D_z c_p) \cdot \nabla_\perp T \\ &\quad + \frac{D_z}{c_p} \sum_{\alpha=1}^{N_s} \left\{ \frac{c_{p,\alpha}}{Le_\alpha} (\nabla_\perp Y_\alpha + Y_\alpha \nabla_\perp \ln W) \right\} \cdot \nabla_\perp T, \end{aligned} \quad (15a)$$

$$\begin{aligned} \mathcal{J}_5^\perp &= -\frac{\varepsilon^\perp}{\rho} \frac{\partial T}{\partial Z} \\ &= -\frac{1}{Z_1 - Z_0} \sum_{\beta=1}^{N_e} \gamma_\beta \sum_{\alpha=1}^{N_s} \frac{n_{\alpha\beta} W_\beta}{W_\alpha} \left\{ \frac{D_z}{Le_\alpha} (\nabla_\perp \cdot \nabla Z) \left(\frac{\partial Y_\alpha}{\partial Z} + Y_\alpha \frac{\partial \ln W}{\partial Z} \right) \right. \\ &\quad \left. + \frac{D_z}{Le_\alpha} \nabla Z \cdot \frac{\partial}{\partial Z} (\nabla_\perp Y_\alpha + Y_\alpha \nabla_\perp \ln W) \right. \\ &\quad \left. + \frac{1}{\rho} \nabla_\perp \cdot \left[\frac{\rho D_z}{Le_\alpha} (\nabla_\perp Y_\alpha + Y_\alpha \nabla_\perp \ln W) \right] \right\} \frac{\partial T}{\partial Z} \\ &\quad + D_z (\nabla_\perp \cdot \nabla Z) \frac{\partial T}{\partial Z}. \end{aligned} \quad (15b)$$

Following the same convention, the preferential diffusion term, introduced in Section 3.1, has been decomposed into a flame-aligned, \mathcal{E}^z , and a flame-orthogonal part, \mathcal{E}^\perp . These contributions are contained in the \mathcal{J}_5 terms. It is noted that, by omitting the preferential diffusion and all flame-orthogonal terms, Eq. (13) with (14) are identical to that derived by Pitsch and Peters [4].

The terms in Eq. (15) account for the flamelet interaction. So far, the significance of all these non-local contributions on the flame evolution has not been fully investigated. The only term that has been considered is the \mathcal{J}_4 contribution, which represents the collective effects of lateral diffusion along the mixture fraction isosurface and curvature. The relevance of the initial phenomenon on the flame reignition was investigated by Sripakagorn et al. [24] in the context of a DNS-study, consisting of a fully-developed homogeneous and isotropic turbulent field with constant thermo-viscous properties and single-step reversible chemistry.

To investigate the relevance of the flame-orthogonal contributions, we extract all terms of Eq. (13) from the DNS-database. To this end, all derivatives along the curvilinear flamelet coordinate direction are computed as $\partial/\partial Z = \frac{\hat{\mathbf{n}}}{|\nabla Z|} \cdot \nabla$, and derivatives in flame-orthogonal direction are evaluated using the identity $\nabla_\perp = \nabla - \nabla Z \partial/\partial Z$.

At this point, we would like to remind the readers that the flamelet Eq. (13) is exact, since it is a direct result of transforming Eq. (10) into a flame-local coordinate system (although now written in a rather inconvenient form). Therefore, we can refer to Eq. (13) as the “exact model”, and categorize Eq. (13) with only the flame-aligned contributions (14) as the “first-order model”. Peter’s “classical flamelet model” is then obtained by introducing a closure model for the scalar dissipation rate, by specifying static boundary conditions in the fuel and oxidizer streams, and by representing the flamelet equations in terms of a species-independent mixture fraction.

The objective of the subsequent analysis is then to assess the validity of these individual assumptions and to provide guidance for the applicability of the flamelet model to configurations that are significantly more complex in topology than canonical flames.

4. Results

In the following, results from the *a priori* analysis of the DNS data are presented. This analysis begins with a discussion of the flamelet topology and the spatial structure of the Lagrangian flamelets in this reacting JICF-configuration. By employing the diagnostic tools that were developed in the previous section, a conditional analysis of results for temperature and scalar dissipation rate is performed in Section 4.2. Following the evaluation of temperature and scalar dissipation rate, a detailed investigation of the flamelet budget-terms and their influence on ignition and flame stabilization is presented in Section 4.3.

This investigation is performed in the context of a mixture fraction conditioned analysis by collecting conditional statistics over 490 DNS flow-field results that span approximately two characteristic flow-through-times (here defined with respect to the cross-stream velocity $U_{cf} = 55$ m/s and the extent of the computational domain in the streamwise direction $L_x = 25$ mm). The mixture fraction space is discretized into 600 equally-spaced bins, and all conditional results are denoted by angular brackets. In this context it is noted that the available sample interval is not sufficient to obtain fully converged results due to the presence of large-scale coherent structures in the jet far-field region. An example of this is illustrated by the asymmetric temperature field in Fig. 1b. While a larger sampling interval would increase the statistical convergence, this was shown to be currently not feasible since data storage capacity is limited and the current database already occupies

more than 100 TB in size and requires over 2400 cores to access one instant. Because of this, comprehensive statistical analysis and a *posteriori* study are limited.

4.1. Flamelet topology

In this section, we investigate the flamelet topology and provide a detailed characterization of the flame structure in this complex JICF-configuration. To reveal prevailing differences in the flame topology and underlying combustion-physical processes, we consider different regions in the JICF, corresponding to near-, ignition-, and far-field regions along the windward and leeward sides and the sideline of the transverse jet flame. The positions of these representative conditional averaged flamelets with respect to the mean stoichiometric surface are illustrated in Fig. 3. Detailed illustrations of the flamelet-topology and corresponding flame structure are presented in Figs. 4–6. These results are arranged in columns according to their azimuthal positions, namely the windward side ($\xi = 0$), sideline ($\xi = 0.25$), and the leeward side ($\xi = 0.5$).

Shown in the first row is the conditional averaged flamelet topology and its intersection with the mean stoichiometric mixture fraction isosurface. The temperature along the flamelet-structure is indicated by the color of the symbols, and the conditional velocity field along the flamelet is shown by vectors. For orientation, a reference coordinate system is included.

The second row shows the conditional averaged temperature and arclength ($\langle \zeta \rangle$) of the flamelet with respect to mixture fraction. The location of the stoichiometric mixture is indicated by the vertical dashed line. Components of the mixture fraction-conditioned velocity field along the flamelet are shown in the third row, where $\langle u_z \rangle = \langle \mathbf{u} | Z \cdot \hat{\mathbf{n}} \rangle$ denotes the mean velocity component in the flame-aligned direction, and $\langle u_\perp \rangle = |\langle \mathbf{u} | Z - u_z \hat{\mathbf{n}} \rangle|$ is the resulting velocity component orthogonal to the flamelet. The last row shows conditional mean profiles of scalar dissipation rate, $\langle \chi_z | Z \rangle$, and the most compressive and extensional strain rates, which are denoted by $\langle a_c \rangle$ and $\langle a_E \rangle$, respectively. These quantities correspond to the minimum/maximum eigenvalues that are evaluated from the decomposition of the strain rate tensor, $\mathbf{a} = \frac{1}{2} [\nabla \mathbf{u} + (\nabla \mathbf{u})^T]$.

Figure 4 shows results of the topology analysis at the region of high shear near the nozzle-exit. The extracted flame-topology (first row) shows that all flamelets exhibit insignificant amount of folding, so that the averaged flamelet topology has a quasi one-dimensional structure. A comparison of the temperature and flame-length (second row) in mixture fraction space shows a similar behavior. In this chemically inert region near the nozzle exit, the flamelet structure is controlled by mixing processes. Much information can be discerned from the velocity plot (third row): (i) Relatively insignificant u_z for all three azimuthal positions, suggesting that there is little flow in the flame-aligned direction at the nozzle-near region; (ii) Low-velocity region on the fuel-lean side, which is a consequence of the stagnation flow induced by the interactions of the fuel jet and the crossflow stream; (iii) Noticeable increase in u_\perp at the fuel-rich mixture indicates that the flame-orthogonal velocity component is mostly aligned with the bulk flow of the fuel jet (i.e. the wall-normal direction). Results in the bottom row show that there is a common trend between the scalar dissipation rate and the dominant principal strain, although it is noted that the maximum points of these two quantities do not usually coincide and the strain rate displays a wider structure than the dissipation term; similar observations have been reported in a study on the effects of unsteady strain on scalar dissipation rates by Kothnur and Clemens [25]. It also appears that the principal strain rates have an azimuthal dependence. The most extensional (black dashed line) and the most compressive (black solid line) strains dominate the windward and leeward sides, respectively. This could

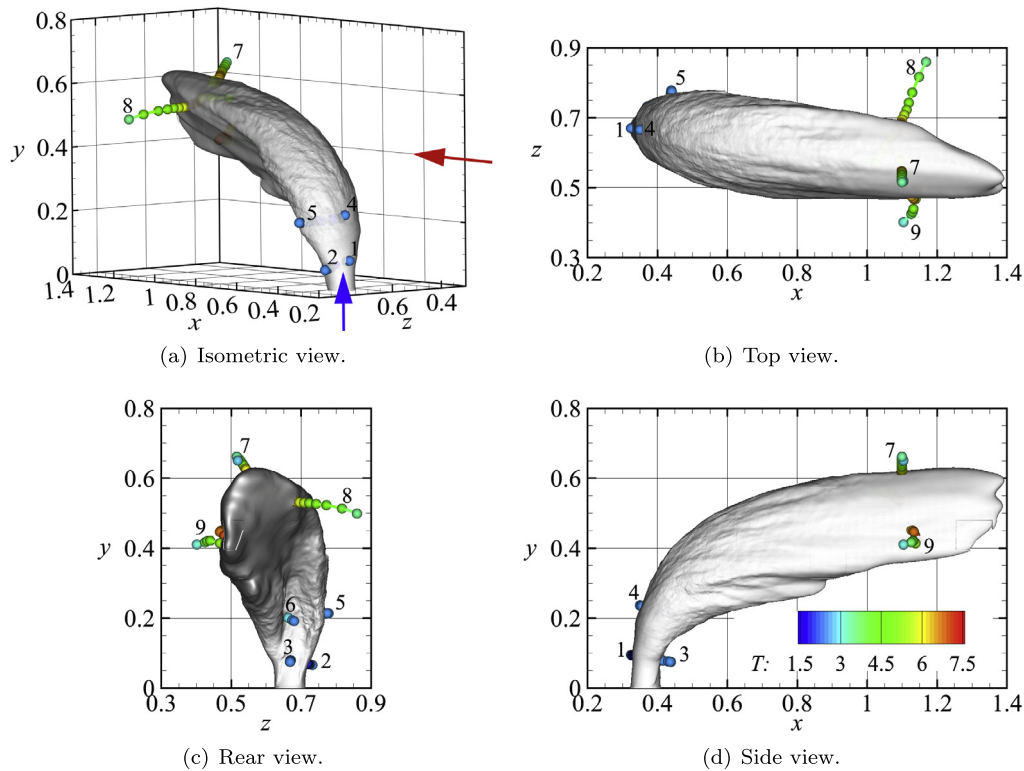


Fig. 3. Locations of the evaluated conditionally averaged flamelets with respect to the mean stoichiometric mixture fraction isosurface. Flamelets are colored by temperature and labeled by a number, ranging from 1 to 9, which is also used in Figs. 4–6; Flamelets 1–3 are in the near-field, 4–6 are in the stabilization-region, and 7–9 are in the far-field. The blue and red arrows in (a) denote the fuel and cross-flow injection directions, respectively. (For interpretation of the references to colour in this figure legend, the reader is referred to the web version of this article.)

be attributed to the high shear at the windward side and strong compression due to vortices at the leeward side. Results for the sideline display comparable strain rate profiles. The leeward fuel-rich region exhibits a compressive strain that is at least twice as strong as the dominating strain rates at other positions.

At the flame-ignition region (approximately $\eta = 0.25$), as shown in Fig. 5, little difference can be observed for all the flamelet structures. For instance, all flamelets exhibit insignificant amount of bending and are distorted only by flame-aligned compression/extension. The most obvious indication for flame ignition is the rise in the maximum leeward temperature, whereas the windward side and sideline continue to sustain the same mixing temperature profile shown in Fig. 4. In contrast to the flamelet profiles in nozzle-near region, the flame-aligned velocity component, u_z , is seen to be relevant at all three azimuthal positions, especially so for fuel-rich mixtures. The alignment of flame-orthogonal velocity and bulk flow of the jet is retained for the windward and leeward sides, while u_{\perp} at the sideline is relatively constant. The correlation between the dominant principal strain and scalar dissipation rates is also obvious, although the distinction between most compressive and most extensional strains has largely diminished. However, it is noted that the most extensional and most compressive strain rates are still the strongest strain at the windward and leeward sides, respectively.

Flamelets at the far-field region are depicted in Fig. 6, where distortions of the flamelets due to both folding and stretching are clearly discernible. These distortions are partially attributed to insufficient temporal sample size, which is expected to be particularly severe at the downstream locations as a result of the large-scale mixing processes and associated large hydrodynamic time-scales. The temperature distribution also differs from the aforementioned mixing profile, corresponding to a reacting profile that approaches the equilibrium solution. The depletion in the

range of mixture fraction is an expected result of mixing of the reactants. According to the velocity plots, it appears that the u_{\perp} -component is much less sensitive to the azimuthal position than the u_z -component, with the former being approximately constant at 0.1 while the latter reduces to zero with increasing ξ (i.e. from windward side to leeward side). Compared to the near-field vicinities, the greatest changes at the far-field region are found in the profiles for strain and dissipation rate terms: (i) the scalar dissipation rate is hardly representative of a Gaussian shape; (ii) the principal strain and scalar dissipation rates are no longer correlated; and (iii) the most relevant strain for all flamelets is compressive in nature. It should also be noted that the magnitudes of strain and dissipation rates reduce by as much as three orders compared to the near-nozzle region.

In summary, in this analysis we extracted the exact flamelet-structure of a topologically-complex JICF configuration in a Lagrangian framework. This analysis showed that the averaged flamelet structure is dominantly quasi one-dimensional, except in the downstream regions where statistical results are not fully converged. Nonetheless, the findings obtained from this investigation are relevant for experimental investigations, suggesting that planar measurements that account for the alignment of the mixture fraction field can provide valuable insights to the flame-topology. The analysis of the flamelet structure in different regions of the flame showed qualitatively different flame-regimes, which are characterized by different velocity and strain rate profiles and resulting ignition scenarios. It will be shown in the subsequent section that this behavior can be represented by the flamelet formulation.

4.2. Mixture fraction conditioned data

In the following, the flame structure of the JICF-configuration is analyzed, and the evolution of the conditional temperature and

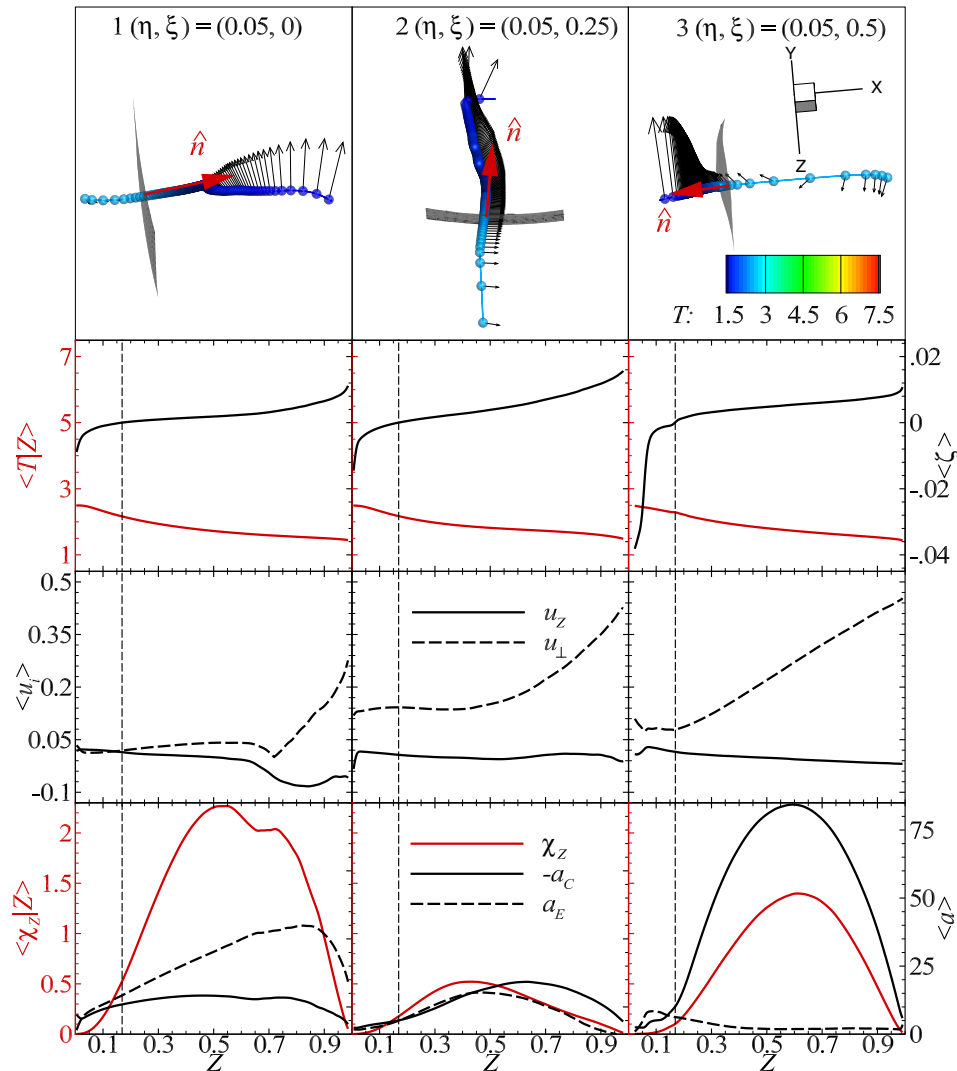


Fig. 4. Flamelet-topology at the nozzle-near region. Velocity vectors are shown by black arrows (scaled relatively by magnitude), and the flame-normal vector (pointing towards the fuel side) is denoted by \hat{n} . Symbols are colored by temperature, and individual flamelets are labeled following the notation in Fig. 3. The vertical dashed line denotes the location of the stoichiometric mixture. Conditional temperature and flame length, velocity components, and scalar dissipation and principal strain rates are shown in the second to fourth rows, respectively.

scalar dissipation rate along the jet trajectory for the following three azimuthal locations along the jet circumference are discussed: $\xi = 0$ (windward), $\xi = 0.25$ (sideline), and $\xi = 0.5$ (leeward).

Ensemble-averaged conditional temperature-profiles at five distinct locations along the jet-trajectory are presented in Fig. 7. For reference, a steady flamelet-profile for equilibrium and unity Lewis-number conditions is shown by a thin black line. This comparison with the flamelet solution is appropriate, since later results in Section 4.3 will demonstrate that preferential diffusion effects are negligible at downstream locations. It can be seen that the one-dimensional temperature profiles prior to $\eta = 0.25$ are qualitatively similar for all azimuthal directions, since there is no reaction occurring at these nozzle-near regions. However, these non-reacting temperature profiles are not linear and have some amount of convexity due to variations of specific heat on mixture fraction space. At $\eta = 0.25$, the temperature distribution at the leeward side increases prominently, while that at the windward and sideline locations remain close to the earlier mixing profile. At $\eta = 0.5$, it can be seen that the temperature profiles at sideline and leeward locations are well above the mixing profile, whereas

that at the windward side exhibits a slower ignition transition. This lift-off distance is consistent with previous findings by Grout et al. [16], and is also seen in Fig. 1a. All temperature profiles at the three azimuthal locations, $\xi = 0, 0.25$, and 0.5 , peak around the vicinity of the stoichiometric mixture fraction at $\langle T|Z \rangle \approx 6.6, 7$, and 7.2 , respectively.

The evolution of the conditionally-averaged scalar dissipation rate along the jet trajectory is presented in Fig. 8. Results for the jet sideline and leeward side show that the dissipation rate at Z_{st} decreases monotonically along the jet trajectory. This is in contrast to the windward side for which $\langle \chi_z|Z_{st} \rangle$ exhibits a sharp increase beyond $\eta = 0.1$. This peak location corresponds to the region of largest shear between fuel-jet and approaching air stream from the transverse oxidizer jet (cf. Fig. 1a). In this context it is noted that the dissipation rate profiles are mostly skewed toward the fuel-rich side, and this becomes more pronounced with increasing distance along the jet-trajectory. This is emphasized by plotting the analytic dissipation rate profile for a counter-flow diffusion flame [3] at quenching condition (denoted by “Qch”) in Fig. 8.

The analysis of the dissipation rate profiles on the leeward side provides some indications for the ignition and the flame-stabilization

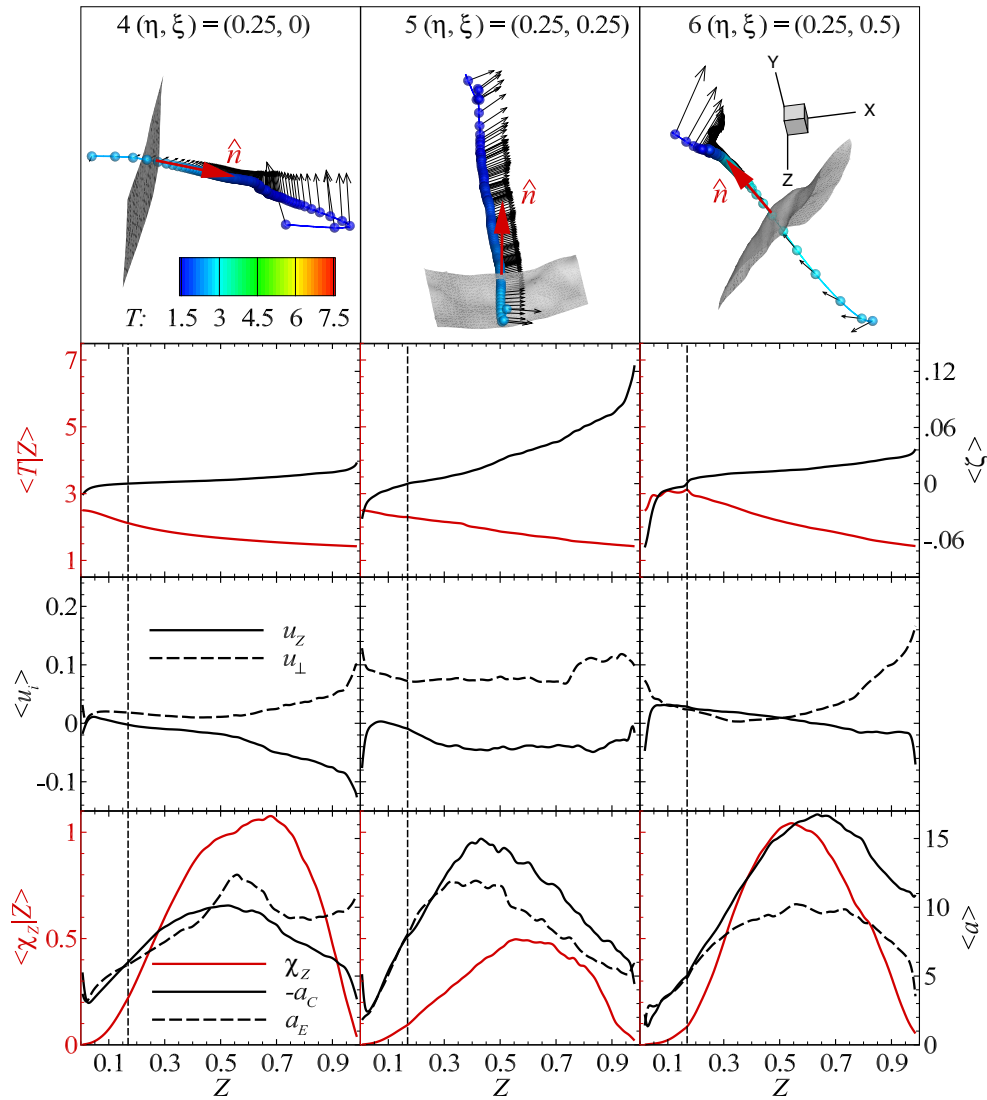


Fig. 5. Flamelet topology at the leeward flame-ignition region. See Fig. 4 for description.

mechanism. In particular, it can be seen from Fig. 8c that the scalar dissipation rate on the fuel-lean side remains below the theoretical quenching dissipation rate (“Qch”) for $\eta \geq 0.1$. Such conditions favor flame stabilization, potentially contributing to the shorter lift-off distance at the leeward side. In contrast, the peak location of the scalar dissipation rate profile at the sideline is seen to shift to the fuel-lean side at $\eta = 0.1$, which can be attributed to a shift in the scalar mixing characteristics with increasing downstream distance. As a result, the scalar dissipation rate for $Z < Z_{st}$ at the sideline only falls below the quenching profile for $\eta \geq 0.25$. Interestingly, it is noted that the windward dissipation rate profile will only cross the theoretical quenching dissipation rate at $0.25 < \eta < 0.5$. This is more delayed than the sideline and leeward sides and qualitatively consistent with the flame lift-off distance in the current JICF-configuration.

The evolution of temperature and dissipation rate at the stoichiometric condition along the jet-trajectory η is shown in Fig. 9. Values of high scalar dissipation rate correspond to conditions at the nozzle, and $\langle \chi_z | Z_{st} \rangle$ decreases with increasing distance along η . For reference, the so-called “S”-shaped curve, obtained from the solution of the steady flamelet equations is shown by the black line. DNS-results at three different azimuthal locations are presented, corresponding to the windward (green dashed-dotted line), sideline (blue dashed line), and leeward (red solid line) positions. It is interesting to note that, in the present conditions, the unstable

middle branch of the “S”-shaped curve is almost horizontal and levels at approximately $T_{st} = 3$. This temperature, as pointed out by Hewson and Kerstein [26], is the crossover temperature, below which chain termination is faster than chain branching. In addition, the flatness of the middle branch indicates the need for an ignition source to initiate chemical reactions, ruling out classical flamelet ignition theory based on autoignitive conditions. This feature is also reflected in the DNS, which employed an external heat source to initiate reaction and flame-anchoring [15].

The conditional flamelet trajectory for $\xi = 0.5$ illustrates a rapid temperature rise at $\langle \chi_z | Z_{st} \rangle \approx 0.1$, which is associated with the early ignition onset at the leeward side of the JICF. As expected, all state-space trajectories defy classical flamelet ignition theory and display an oblique crossing of the unstable middle-branch of the “S”-shaped curve. With increasing downstream distance along the jet-trajectory, all flamelets converge to a stationary point that coincides with the upper stable branch of the steady flamelet solution.

In summary, we have evaluated quantitative results of conditional averaged temperature and scalar dissipation rate at different locations in the jet flame, corresponding to the windward side, sideline, and leeward side of the jet. Early ignition at the leeward side, as compared to the windward side and sideline, is possibly related to a faster reduction in the dissipation rate for $\xi = 0.5$.

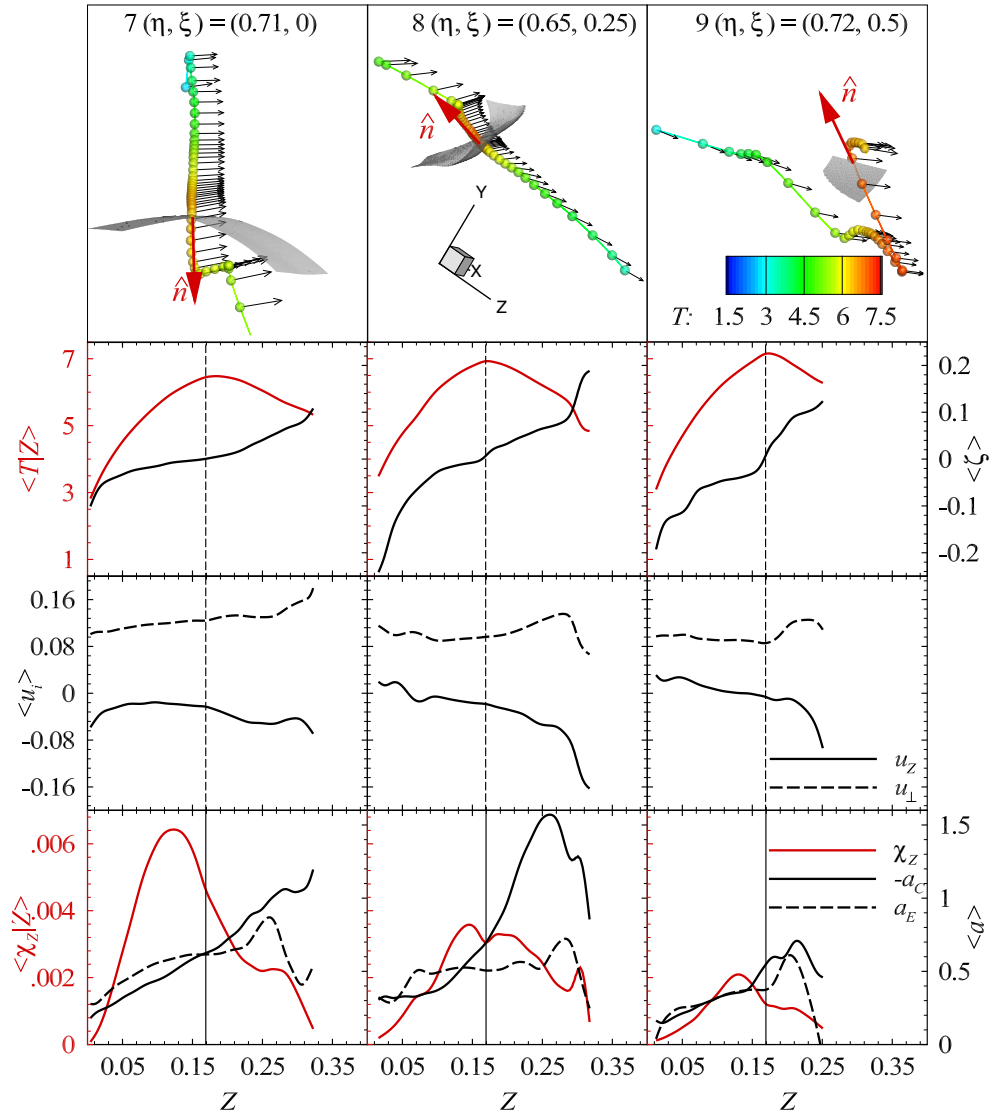


Fig. 6. Flamelet topology at the far-field region. See Fig. 4 for description.

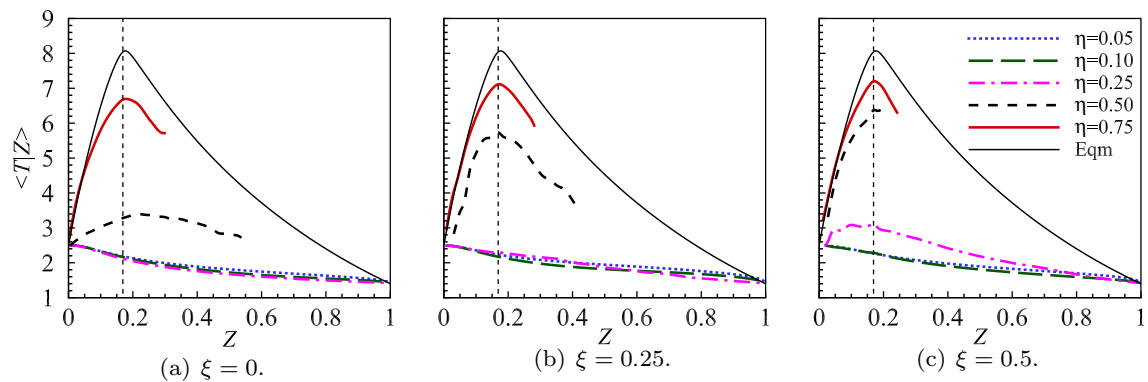


Fig. 7. Conditionally-averaged temperature profiles for (a) $\xi = 0$, (b) $\xi = 0.25$, and (c) $\xi = 0.5$ and different locations along the jet-trajectory. The vertical dashed line indicates the location of stoichiometric mixture.

Comparing state-space trajectories to the “S”-shaped curve, it is seen that these ignition trajectories do not agree with classical flamelet ignition theory. Most importantly, there is an appreciable

azimuthal dependence of these stoichiometric ignition trajectories, clearly differentiating the behavior of the flame at various sides of the jet.

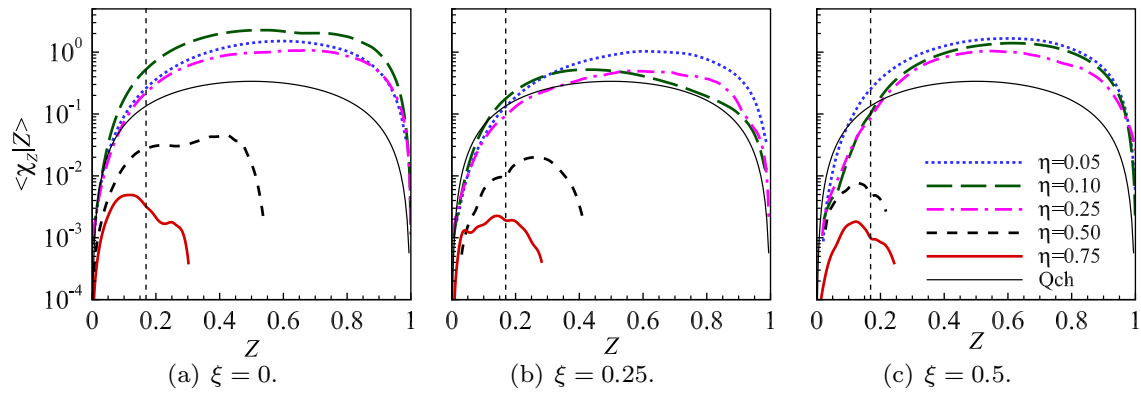


Fig. 8. Conditionally-averaged scalar dissipation rate profile for (a) $\xi = 0$, (b) $\xi = 0.25$, and (c) $\xi = 0.5$ and different locations along the jet-trajectory. The vertical dashed line indicates the location of stoichiometric mixture, and the analytic scalar dissipation rate profile at quenching condition (Qch) is denoted by the thin black line.

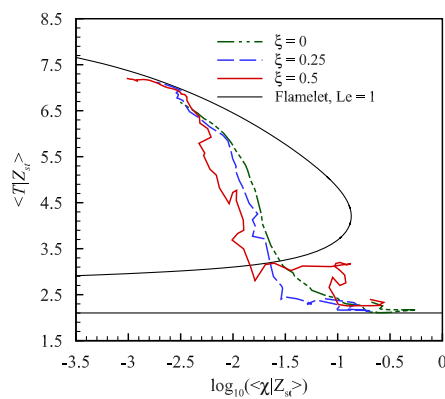


Fig. 9. Spatial evolution of temperature as a function of stoichiometric scalar dissipation rate along jet trajectory η for $\xi = 0$, $\xi = 0.25$, and $\xi = 0.5$. The black line represents the “S”-shaped curve computed from a steady flamelet-formulation considering unity Lewis number.

4.3. Flamelet budget-analysis

After examining conditional results of primitive flow-field quantities, we will next conduct a budget-analysis of the fully expanded temperature-flamelet equation. This investigation is performed by analyzing mean mixture-fraction conditioned quantities of all individual terms in Eq. (13). Five positions along the jet-trajectory, corresponding to a region close to the jet-nozzle exit ($\eta = 0.05$), upstream of the ignition location ($\eta = 0.1$), in proximity to the ignition point ($\eta = 0.5$ and 0.25 for windward and leeward sides, respectively), and near the tip of the flame ($\eta = 0.75$). For reference, these locations are schematically shown in Fig. 1a. Results from the budget-analysis of the temperature equation are illustrated in Fig. 10. Since these terms balance the temporal derivative of temperature, any negative contribution can be understood as a heat-sink term, which delays flame-ignition and combustion. In the following analysis all contributions along the flame-aligned direction are shown by lines, and budget terms in the flame-orthogonal direction are shown by symbols. Note also that collective contributions due to curvature effects and lateral diffusion are negligible throughout this configuration, as indicated by the term $\langle \mathcal{J}_4^Z | Z \rangle$ in all the presented plots. The Lagrangian temporal derivative term, evaluated as the sum of the terms on the RHS of Eq. (13), is shown in Fig. 10 as an indicator to the balance of the budget terms. It is noted that these terms are obtained by applying an Eulerian averaging procedure. As such, any imbalance can then be interpreted as the effect of the Lagrangian unsteadiness.

Results presented in Fig. 10 show that scalar mixing (term $\langle \mathcal{J}_1^Z | Z \rangle$) and enthalpy-flux due to species-diffusion (term $\langle \mathcal{J}_3^Z | Z \rangle$) constitute, to leading-order, effects in the lower region of the flame. We observed that $\langle \mathcal{J}_1^Z | Z \rangle$ is positive in most of the mixture fraction coordinate, which is a behavior consistent with the non-linear mixing temperature distributions shown in Fig. 7. We also note that the flame-aligned preferential diffusion term, $\langle \mathcal{J}_5^Z | Z \rangle$, is non-negligible.

At $\eta = 0.05$, the azimuthal dependence of the budget terms is apparent, with contributions from $\langle \mathcal{J}_1^Z | Z \rangle$, $\langle \mathcal{J}_3^Z | Z \rangle$, and $\langle \mathcal{J}_5^Z | Z \rangle$ being distinctly smaller at the sideline than at the other two sides. This observation indicates the significance of shearing effects that the cross-flow has on the mixing with the fuel stream. However, apart from their absolute magnitudes, it is interesting to note that the terms $\langle \mathcal{J}_1^Z | Z \rangle$, $\langle \mathcal{J}_3^Z | Z \rangle$, and $\langle \mathcal{J}_5^Z | Z \rangle$ also display trends that are independent of the azimuthal position at these three upstream jet-trajectory locations. For instance, it can be discerned that scalar-mixing always has a negative minimum point on the fuel-lean side before increasing to its dominating positive region, while preferential diffusion is transferring heat from the fuel-rich mixture to the fuel-lean side. The enthalpy-flux is consistently negative throughout, serving as the primary mechanism that opposes the heat-addition induced by scalar-mixing.

The azimuthal dependence of the flamelet-budget is particularly prominent at $\eta = 0.1$ (second row). Specifically, there is a general increase in the magnitudes of the various flame-aligned terms for the windward and the sideline locations. Contributions from the mixing and species-induced diffusion at the jet leeward side are almost unchanged compared to their counterparts at $\eta = 0.05$. The maximum point of the flame-aligned preferential diffusion profile is seen to spread across the stoichiometric mixture. In this context, it is noted that the location of $\eta = 0.1$ is critical in determining flame-stabilization. From Fig. 1a it can be deduced that combustion is initiated at the leeward side. In order to understand the underlying physics that sustains the flame in the current setup, we therefore compare the various contributions at different azimuthal locations. It can be seen that the major difference among the different ξ -locations lies in the $\langle \mathcal{J}_5^Z | Z \rangle$ -distribution, which has been discussed previously.

From the budget-analysis at the location of $\eta = 0.25$, it can be seen that the heat-release term $\langle \mathcal{J}_2^Z | Z \rangle$ is apparent at both leeward and sideline sides. On the other hand, the windward side remains non-reactive at this η -location, while the other flamelet contributions exhibit a general decay in their absolute magnitudes. It is interesting to note that these budget terms remain unchanged in their relative magnitudes, suggesting the existence of a consistent pattern in the non-reacting flamelet budgets.

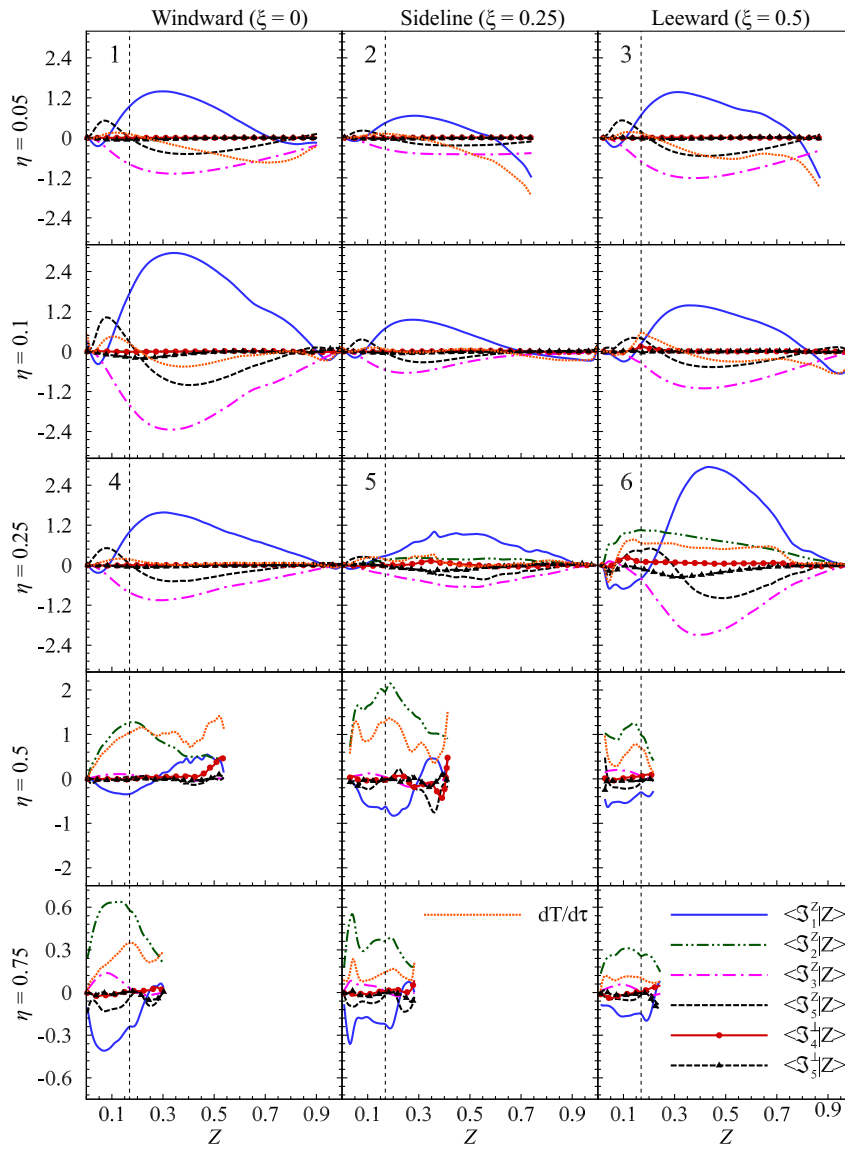


Fig. 10. Budget-analysis of the temperature flamelet Eq. (13). Columns show three azimuthal positions, and rows correspond to locations along the jet-trajectory. Labeled flamelets correspond to those shown in Fig. 3. The vertical dashed line indicates the location of the stoichiometric mixture fraction. All budget terms are mixture-fraction conditioned results.

Dramatic changes in the budget are first observed at $\eta = 0.5$ (fourth row), where the various contributions at all azimuthal locations of the same cross-sectional plane no longer show any structural similarity. Most prominent is the growth in $\langle \mathcal{J}_2^Z | Z \rangle$, which

has become the leading-order term, indicating successful flame-ignition and flame-stabilization. We can see a decay in the contributions from species-induced diffusion and preferential diffusion.

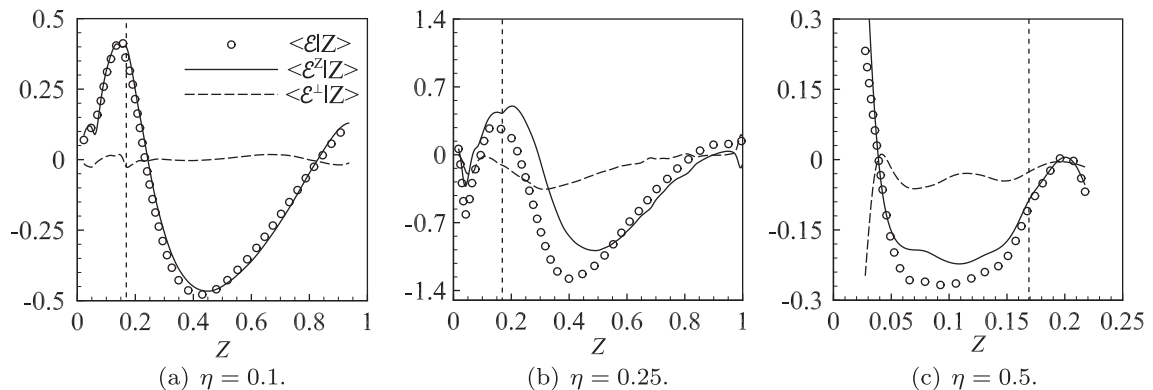


Fig. 11. Decomposition of the total preferential diffusion term at the leeward side of the flame at three locations along the jet trajectory: (a) $\eta = 0.1$, (b) $\eta = 0.25$, and (c) $\eta = 0.5$. The open symbols correspond to the total preferential diffusion term, and the terms $\langle \mathcal{E}^+ | Z \rangle$ and $\langle \mathcal{E}^- | Z \rangle$ are shown by solid and dashed curves, respectively.

The budget-analysis at $\eta = 0.75$ is shown in the last row of Fig. 10, and the following observations can be made: (i) due to the enhanced mixing of reactants, the flamelet structures span a smaller range in mixture fraction space than seen at other jet-trajectory locations; (ii) the reduction in magnitude of all terms in the flamelet equation indicates that the flame is approaching the equilibrium condition; and (iii) contributions due to preferential diffusion become insignificant, so that the flame-structure in the equilibrium regime can be represented by a unity Lewis-number formulation. Furthermore, from the approximate balance of all the terms, it appears that any transient effects at this far-field region are negligible.

For its pertinent role in affecting flame-ignition and flame-stabilization, the preferential diffusion term, \mathcal{E} , requires further analysis. To this end, the leeward preferential diffusion term and its decomposition into flame-aligned and flame-orthogonal directions are evaluated at three locations on the jet-trajectory. These results are presented in Fig. 11, showing that preferential diffusion effects occur predominantly in the flame-aligned direction, since $\langle \mathcal{E}|Z \rangle$ and $\langle \mathcal{E}^2|Z \rangle$ are in good agreement. This observation is general and also applies to other locations in the JICF, as can be observed from Fig. 10, where the $\langle \mathcal{J}_5^\pm|Z \rangle$ term is effectively negligible. This finding is encouraging for practical applications since it confirms that only the consideration of the term \mathcal{E}^2 is required in order to represent preferential diffusion effects. Therefore, this analysis shows that non-unity Lewis number effects in the flame-aligned direction are crucial in strengthening the flame. In fact, such effects are not uncommon and have been investigated in various studies [27,28]. It should be cautioned, however, that this correlation between flame-ignition and preferential diffusion effects might be specific to the present JICF-configuration, since H_2 is known to induce strong non-unity Lewis-number effects.

In this context it is noted that all results are conditioned on mixture fraction and have been ensemble-averaged. Therefore, there will be no unclosed terms in our analysis because the conditional averaged non-linear quantities are evaluated as a whole. This is consistent with our objective to investigate fundamental model assumptions associated with the flamelet formulation, and the aspect of the flamelet closure modeling is subject of future work.

In summary, this budget-analysis shows that the flame-structure is controlled by first-order expansion terms arising from scalar-mixing (\mathcal{J}_1^2), heat-release rate (\mathcal{J}_2^2), species-diffusion induced enthalpy-flux (\mathcal{J}_3^2), and preferential diffusion (\mathcal{J}_5^2). Given the complexity of this configuration, it is encouraging that the flamelet-paradigm [2] remains on average valid. However, it should be recognized that higher-order effects due to flame curvatures and lateral diffusion of heat have not been fully explored in this study. An interesting analysis in the future will be to investigate the influence that these flame-orthogonal terms have on the conditional fluctuations of temperature and species, which in turn have non-linear contributions on the heat-release rate. Currently, such effects have been collapsed onto the heat-release term.

5. Conclusions

An *a priori* study of the flamelet model was performed with the specific objective of investigating fundamental model assumptions associated with the asymptotic flamelet expansion, the omission of higher-order expansion terms, and the one-dimensional flamelet-representation. To this end, a reactive jet-in-cross-flow configuration was considered, exhibiting considerable complexities due to both the underlying flow-field and its coupling with combustion processes (such as stratification, strong shear and recirculation regions, and large-scale flame-vortex coupling) beyond those

found in canonical and convectively one-dimensional flame configurations. In this analysis, diagnostic was developed to extract the local and instantaneous flamelet topology by introducing a flame-local coordinate system defined with respect to the mean stoichiometric surface of the JICF.

All terms in this analysis of the temperature flamelet equation were evaluated including contributions in flame-aligned and flame-orthogonal directions. The analysis showed that the local flamelet structure is dominantly quasi one-dimensional, except in downstream regions of the JICF because of insufficient temporal samples for statistical convergence.

A detailed budget-analysis was performed to show that contributions from heat-release, diffusion, and species-diffusion-induced enthalpy flux along the flame-aligned direction have major effects on the flamelet equation, while the flame-orthogonal terms are on average negligible. The flame-aligned preferential diffusion effect was found to be crucial and favor ignition and flame-stabilization. These contributions can be considered by extending the flamelet model, for instance, by considering non-unity Lewis-number effects [4] and by solving the unsteady flamelet equations. The subjects of closure-modeling and dependence on conditional fluctuations have not been addressed in the work, and will be the scope of future research.

Acknowledgments

Financial support through the Air Force Office of Scientific Research under Award No. FA9550-11-1-0031 and through the Department of Energy University Turbine Systems Research program under Award No. DE-FE0007060 are gratefully acknowledged. We would like to thank Yee Chee See for discussions on the generalized coordinate transformation and conditional data analysis. We thank an anonymous reviewer for helpful comments on the Lagrangian flamelet formulation.

The work at Sandia National Laboratories (SNL) was supported by the Division of Chemical Sciences, Geosciences, and Biosciences, Office of Basic Energy Sciences of the US Department of Energy. SNL is a multiprogramme laboratory operated by Sandia Corporation, a Lockheed Martin Company, for the US DOE under contract DE-AC04-94AL85000. Computational support and resources were provided by the National Center for Computational Sciences at Oak Ridge National Laboratory, which is supported by the Office of Science of the US Department of Energy under contract DEAC05-00OR22725.

References

- [1] N. Peters, *Combust. Sci. Technol.* 30 (1983) 1–17.
- [2] N. Peters, *Prog. Energy Combust. Sci.* 10 (3) (1984) 319–339.
- [3] N. Peters, *Turbulent Combustion*, Cambridge University Press, 2000.
- [4] H. Pitsch, N. Peters, *Combust. Flame* 114 (1998) 26–40.
- [5] C. Kortschik, S. Honnet, N. Peters, *Combust. Flame* 1142 (2005) 140–152.
- [6] H. Xu, F. Hunger, M. Vascellari, C. Hasse, *Combust. Flame* 160 (2013) 2540–2558.
- [7] C. Hasse, N. Peters, *Proc. Combust. Inst.* 30 (2005) 2755–2762.
- [8] D.J. Cook, H. Pitsch, J.H. Chen, E.R. Hawkes, *Proc. Combust. Inst.* 31 (2007) 2903–2911.
- [9] M. Ihme, Y.C. See, *Proc. Combust. Inst.* 33 (2010) 1309–1317.
- [10] V. Mittal, H. Pitsch, A flamelet model for premixed combustion under variable pressure conditions, *Proc. Combust. Inst.* 34 (2013) 2995–3003.
- [11] M. Ihme, H. Pitsch, *Phys. Fluids* 20 (2008) 055110.
- [12] B. Cuenot, F.N. Egolfopoulos, T. Poinot, *Combust. Theory Model.* 4 (1) (2000) 77–97.
- [13] H. Pitsch, *Combust. Flame* 123 (3) (2000) 358–374.
- [14] M. Ihme, Y.C. See, *Combust. Flame* 157 (2010) 1850–1862.
- [15] R.W. Grout, A. Gruber, C.S. Yoo, J.H. Chen, *Proc. Combust. Inst.* 33 (2011) 1629–1637.
- [16] R.W. Grout, A. Gruber, H. Kolla, P.-T. Bremer, J.C. Bennett, A. Gyulassy, J.H. Chen, *J. Fluid Mech.* 706 (2012) 351–383.
- [17] T.F. Fric, A. Roshko, *J. Fluid Mech.* 279 (1994) 1–47.
- [18] J. Li, Z. Zhao, A. Kazakov, F.L. Dryer, *Int. J. Chem. Kinet.* 36 (2004) 566–575.

- [19] R.W. Bilger, S.H. Starner, R.J. Kee, *Combust. Flame* 80 (1990) 135–149.
- [20] J.C. Sutherland, P.J. Smith, J.H. Chen, *Combust. Theory Model.* 9 (2) (2005) 365–383.
- [21] J.H. Chen, A. Choudhary, B. de Supinski, M. DeVries, E.R. Hawkes, S. Klasky, W.K. Liao, K.L. Ma, J. Mellor-Crummey, N. Podhorszki, R. Sankaran, S. Shende, C.S. Yoo, *Comput. Sci. Disc.* 2 (2009) 015001.
- [22] C.H. Gibson, *Phys. Fluids* 11 (1968) 2305–2315.
- [23] A.Y. Klimenko, *Combust. Theory Model.* 5 (2001) 275–294.
- [24] P. Sripakagorn, S. Mitarai, G. Kosály, H. Pitsch, *J. Fluid Mech.* 518 (2004) 231–259.
- [25] P.S. Kothnur, N.T. Clemens, *Phys. Fluids* 17 (2005) 125104.
- [26] J.C. Hewson, A.R. Kerstein, *Combust. Theory Model.* 174 (2002) 35–66.
- [27] J.S. Kim, F.A. Williams, *J. Eng. Math.* 31 (1997) 101–118.
- [28] O. Gicquel, D. Thévenin, N. Darabiha, *Flow Turb. Combust.* 73 (2004) 307–321.